NDT and E International 99 (2018) 64–71

Contents lists available at ScienceDirect

NDT and E International

journal homepage: www.elsevier.com/locate/ndteint

The sizing of small surface-breaking fatigue cracks using ultrasonic arrays

Chaoyong Peng[a,b,*], Long Bai[b], Jie Zhang[b], Bruce W. Drinkwater[b]

[a] School of Physical Science and Technology, Southwest Jiaotong University, Chengdu, 610031, China
[b] Department of Mechanical Engineering, University of Bristol, University Walk, Bristol, BS8 1TR, UK

ARTICLE INFO

Keywords:
Ultrasonic arrays
Defect sizing
Defect characterisation
Fatigue crack
Total focusing method
Scattering coefficient matrix

ABSTRACT

Using ultrasonic arrays to detect and characterise surface breaking cracks is important in the non-destructive evaluation (NDE) field. It can provide early warning of failure and useful information for component integrity assessment. Typically, cracks are approximated by machined slots and used to examine and assess defect detection and characterisation methods. In this paper, real surface breaking cracks are fabricated in 3-point bending specimens following ASTM standard E1820 and used to examine the performance of two array defect characterisation methods: image-based and scattering matrix sizing. In both cases, an array is used to record the full matrix capture (FMC). In image-based sizing, the total focusing method (TFM) is used to form an image from which the defect size is measured directly. This approach is shown to work well for cracks greater than two wavelengths in size. The FMC is also used to extract the defect scattering matrix which is then compared to a pre-computed smooth-crack scattering matrix database. The best match between experiment and this database is found by cross-correlation and used to characterise the defect. This approach is shown to work well for defects in the range of 0.78–1.84 wavelengths. Within these ranges of applicability, both methods show excellent agreement between the known crack length and that measured ultrasonically, with errors less than 19% in all cases.

1. Introduction

Surface breaking cracks (SBCs) resulting from cyclic loading and harsh operating conditions are common in solid structures such as rail tracks, gears, pressure vessels and pipelines [1–6]. Using structural integrity assessment, combined with fracture mechanics calculations, the measured size of SBCs can be used to estimate the remaining life of the structure [7]. In non-destructive evaluation (NDE), there various techniques used to detect the indication of SBCs, for example, dye penetrant inspection, magnetic particle inspection, eddy current testing and thermography [8]. These techniques allow sizing if SBCs are on the accessible front surface of the test structure.

For detecting and sizing SBCs on the inaccessible back surface of components, ultrasonic guided wave or bulk wave inspection can be used. The guided waves technique is typically used to detect and size relatively large defects over a long distance [9–12]. Higher resolution, local inspection can be achieved using ultrasonic bulk wave inspection. Using these approaches, defect detection and characterisation measurements are often made by placing an oblique incidence bulk wave transducer or array on the front-wall of a structure to detect defects on the back-wall [13–29]. Array images can be formed either by traditional imaging approaches [13,14] or via recording the Full Matrix Capture (FMC) and application of post-processing techniques, e.g., the Total Focusing Method (TFM) [15] and its variants [16–18]. An important benefit of using ultrasonic arrays to detect and characterise SBCs is that one array transducer allows a given crack to be illuminated from a wide range of angles. The high resolution images formed increase the chances of detection [15,21] and the data can be further processed to extract the scattering behaviour which provides valuable characterisation information via the scattering coefficient matrix (S-matrix) [20,22]. For a defect with a size greater than approximately two wavelengths it has been shown that information contained within a TFM image can be used to measure crack size [13,18,23]. However, to date this approach has often been shown quantitatively using artificially machined notches [18], simulated rough defects [24] and large embedded real cracks [25,26], whose sizes are greater than 2.5 mm (2 wavelengths at 5 MHz). Alternatively, for cracks less than two wavelengths, it has been shown that the extracted S-matrix can be used for sizing [19,22,23] although this approach has only been experimentally explored on EDM notches whose sizes range from 1 mm to 3 mm (0.8–2.5 wavelength at 5 MHz).

In this paper we examine the performance of defect characterisation using array image-based and S-matrix based sizing techniques. In particular we explore their applicability to real SBCs grown in aluminium samples under 3-point bending. We consider inaccessible back-surface cracks for which bulk wave ultrasonic is the industry standard

* Corresponding author. School of Physical Science and Technology, Southwest Jiaotong University, Chengdu, 610031, China.
E-mail addresses: pengmd@163.com (C. Peng), lb13340@bristol.ac.uk (L. Bai), j.zhang@bristol.ac.uk (J. Zhang), b.drinkwater@bristol.ac.uk (B.W. Drinkwater).

https://doi.org/10.1016/j.ndteint.2018.06.005
Received 11 March 2018; Received in revised form 26 June 2018; Accepted 27 June 2018
Available online 28 June 2018

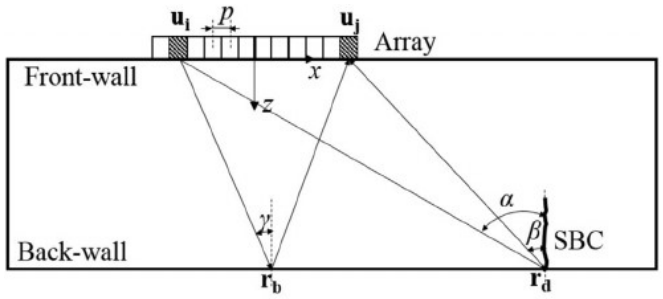

Fig. 1. Schematic diagram illustrating the geometry used in the hybrid forward scattering model.

technique [13,14,25]. The motivation is therefore to understand the measurement limitations of these new techniques on real defects and to assess if they offer advantages over the best existing techniques. This investigation on realistic defects therefore provides a further step towards the industrial uptake of these emerging techniques.

2. Modelled structure and S-matrix

2.1. Overview of the hybrid scattering model

In order to understand the performance of ultrasonic imaging of SBCs and explore methodologies for sizing them, a 2D hybrid scattering model [16,30] was used to simulate array data sets from a simple plate-like structure with a SBC. Here, a hybrid model is used to simulate the ultrasonic waves transmitted from each array element, propagating in a plate-like structure, interacting with both a planar back-wall surface and a SBC, and then received by the array elements.

Consider a 2D solid structure with the geometry shown in Fig. 1. The structure has isotropic material properties defined by the density ρ, longitudinal wave speed c_l and transverse wave speed c_t. Cartesian coordinates, (x, z), represent lateral position and depth with respect to the center of the 1D linear array. The figure also schematically shows two possible wave paths from a transmitter element located at $\mathbf{u_i}$ back to a receiver element located at $\mathbf{u_j}$. One wave path corresponds the wave reflected from the back-wall and it is reflected at $\mathbf{r_b}$ with the same incident and reflected angle γ with respect to the normal of the planar back-wall. The other wave path represents the scattered wave from the SBC at $\mathbf{r_d}$ with the incident angle, α, and the scattered angle, β, with respect to the normal of the planar back-wall. γ is a function of $\mathbf{u_i}$, $\mathbf{u_j}$ and $\mathbf{r_b}$ while α and β are the functions of $\mathbf{u_i}$, $\mathbf{u_j}$ and $\mathbf{r_d}$. Note that in this simulation, only the ultrasonic waves from longitudinal incident, reflected and scattered wave modes were considered although the SBC scattering matrix calculation solved the 2D elastodynamic scattering problem [10,20].

2.2. The far field defect S-matrix

The interaction between ultrasonic waves and a defect is encoded by its far field S-matrix which is defined as the far field complex amplitude of the signals from the crack as a function of the incident and scattered angles (α, β) [22,30,31]. When a plane wave of displacement amplitude u_{in} and propagation angle, α, is incident on a 2D SBC of length, a, the scattered field decays in inverse proportion to the square root of the distance from the crack in the far field. If the amplitude of the scattered wave at a distance r_{sc} along the scattered angle, β, is u_{sc}, then the far field S-matrix is given by Refs. [22,30],

$$S(a,\ f,\ \alpha,\ \beta) = \frac{u_{sc}}{u_{in}}\sqrt{\frac{r_{sc}}{\lambda}}\,exp(-ik(r_{sc}-\lambda)), \tag{1}$$

where, λ is the wavelength and k is the wavenumber ($k = 2\pi/\lambda$). In this paper, a numerical method using local FE modelling without absorbing regions [31] was used to simulate the scattering coefficient matrices (S-matrices) from various vertical smooth SBCs.

2.3. Hybrid forward model to simulate the scattered signals from a structure

The array data is predicted using the above discussed numerically calculated scattering matrix in combination with a classic frequency domain, linear systems model of the wave propagation [16,30]. For a SBC with a length a and located at $\mathbf{r_d}$ as shown in Fig. 1, in the frequency domain, the matrix of raw array data from this defect, $G_{ij}(f)$, received by the array element located at $\mathbf{u_j}$ when the element transmits at $\mathbf{u_i}$ can be written in the following general form [16,30],

$$G_{ij}^{d}(a,\ f,\ \mathbf{u_i},\ \mathbf{u_j},\ \mathbf{r_d}) = \frac{A(f)D(f,\ \alpha(\mathbf{u_i},\ \mathbf{r_d}))D(f,\ \beta(\mathbf{u_j},\ \mathbf{r_d}))S(a,f,\alpha(\mathbf{u_i},\ \mathbf{r_d}),\ \beta(\mathbf{u_j},\ \mathbf{r_d}))exp(ik(|\mathbf{u_i}-\mathbf{r_d}|+|\mathbf{u_j}-\mathbf{r_d}|))}{\sqrt{|\mathbf{u_i}-\mathbf{r_d}||\mathbf{u_j}-\mathbf{r_d}|}}, \tag{2}$$

where, the function $A(f)$ represents the combination of the frequency spectrum of the signal transmitted from the array controller instrument, D is the directivity of an array element [32].

Also shown in Fig. 1 is the wave path for a specular reflection from the planar back-wall of the sample occurring at position $\mathbf{r_b}$. In the frequency domain, the corresponding expression for the first back-wall echo is [16,30],

$$G_{ij}^{b}(f,\ \mathbf{u_i},\ \mathbf{u_j},\ \mathbf{r_b}) = \frac{A(f)D^2(f,\ \gamma(\mathbf{u_i},\ \mathbf{u_j},\ \mathbf{r_b}))R(\gamma(\mathbf{u_i},\ \mathbf{u_j},\ \mathbf{r_b}))exp(ik(|\mathbf{u_i}-\mathbf{r_b}|+|\mathbf{u_j}-\mathbf{r_b}|))}{\sqrt{|\mathbf{u_i}-\mathbf{r_b}|+|\mathbf{u_j}-\mathbf{r_b}|}}, \tag{3}$$

where, R is the longitudinal-longitudinal reflection coefficient [33]. Hence, the total array data from a SBC and the first back-wall reflection, $G(f,\ \mathbf{u_i},\ \mathbf{u_j})$, is,

$$G_{ij}(a,f,\mathbf{u_i},\mathbf{u_j}) = G_{ij}^{d}(a,f,\mathbf{u_i},\mathbf{u_j},\mathbf{r_d}) + G_{ij}^{b}(f,\mathbf{u_i},\mathbf{u_j},\mathbf{r_b}). \tag{4}$$

The time domain data, $g_{ij}(t) = g_d(t) + g_b(t)$, can then be obtained using an inverse Fast Fourier Transform (IFFT) to build up a full simulated FMC data set for a SBC.

3. Sizing methodology for SBCs

Here, the image-based and S-matrix sizing methods are first explored on simulated array data using the hybrid model described briefly in section 2. The TFM [15] was chosen as an example of an ultrasonic array imaging algorithm for image-based sizing of SBCs. For a large SBC, the crack tip and crack mouth can be resolved in the ultrasonic image and hence the crack length can be measured [18]. However, for a small crack these image features merge and a single high intensity region close in shape to the point spread function (PSF) of the array imaging system is observed which is not suitable for sizing.

In the S-matrix sizing technique [22] the S-matrix of the crack is first extracted from the FMC array data set and then used to compare with a pre-computed smooth-crack S-matrix database. The best match between experiment and this database is found by cross-correlation and used to characterise the defect.

In the simulations, an ultrasonic array (i.e. #1 in Table 1) was placed on the front-wall of an aluminium plate of thickness 40 mm, longitudinal velocity c_l = 6400 m/s, transverse velocity c_t = 3100 m/s and density ρ = 2700 kg/m^3.

3.1. Image-based sizing technique

Fig. 2(a) and (b) compare the simulated TFM images for

Table 1
Specification of the array transducers used in simulations and experimental measurements.

Array label	Number of elements, N	Central frequency (MHz)	Element width (mm)	Element pitch p (mm)	Element length (mm)
#1	64	5	0.5	0.6	10
#2	128	10	0.25	0.3	10
#3	64	2.5	0.35	0.5	15

$a = 0.64$ mm (0.5λ at 5 MHz) and $a = 5.12$ mm (4λ at 5 MHz) long, SBCs. In the TFM image of the $a = 0.5\lambda$ crack (Fig. 2(a)), the crack tip and crack mouth are merged while they are separated for the image of the 4λ crack (Fig. 2(b)). Fig. 2(c) shows the image amplitude along a slice through the crack location from which amplitude peaks corresponding to the crack tip and crack mouth can be observed for the larger cracks leading to accurate sizing as seen in Fig. 2(d). However, for the smaller cracks ($a \leq 2\lambda$), the crack tip is not distinct and this limits the image-based sizing technique to $a > 2\lambda$.

3.2. S-matrix sizing method

Fig. 3(a) and (b) show the absolute values of the simulated S-matrices for $a = 0.64$ mm (0.5λ at 5 MHz) and $a = 2.56$ mm (2λ at 5 MHz) SBCs respectively. Note that only part of S-matrix can be extracted from a single FMC data-set due to the angular coverage of the specific array inspection configuration. Fig. 3(c) and (d) show the corresponding extracted S-matrices (see Ref. [22] for fuller details) for array #1 when the crack is located at $(x, z) = (40, 40$ mm). By comparing Fig. 3(c) with 3(d), it can be seen that the smaller crack exhibits more uniform scattered amplitudes over a wider range of angles. The shape variation of the S-matrices with crack length then forms the basis of the S-matrix sizing technique.

In the experimental measurement, once the location of the crack and back-wall are found from the image, the incident and scattered angles from each element to the crack, as well as the expected arrival

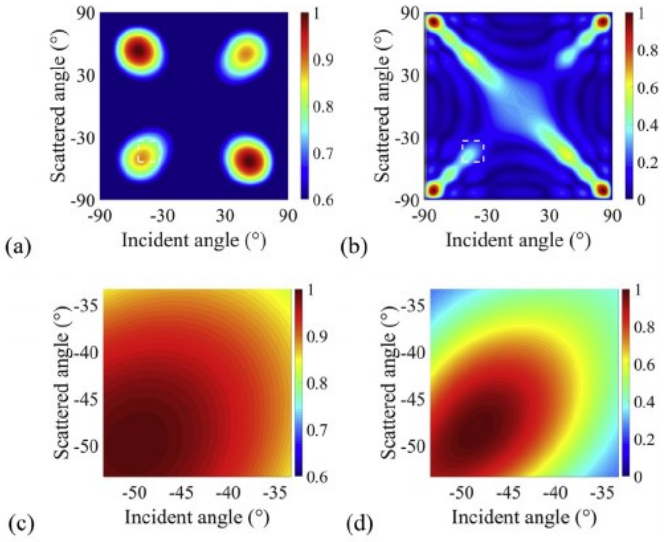

Fig. 3. The absolute values of the simulated S-matrix for a vertical SBC with length of; (a) a = 0.5λ and (b) a = 2λ. The absolute values of the extracted S-matrix for the SBC corresponding to; (c-d) (a-b). It is noted that the amplitude in each figure is normalized to the maximum amplitude.

times from each array element to the crack, can be calculated. To extract the S-matrix from the experimental FMC data we use the sub-array approach (see Ref. [17] for full details). Each component (i.e. a given incident and scattered amplitude) in the measured sub-array S-matrix is the TFM image corresponding to those sub-apertures, (8-element sub-array apertures used in this paper). It is noted that the sub-array S-matrix is a "smoothed" version of the true scattering matrix. However, the key advantage of the sub-array S-matrix is that it provides a route to spatial selectivity and hence reduces S-matrix contamination from nearby features and material noise [22]. For best performance, the pre-computed database of smooth-crack S-matrices is also converted into a sub-array version. The best match between the experimental

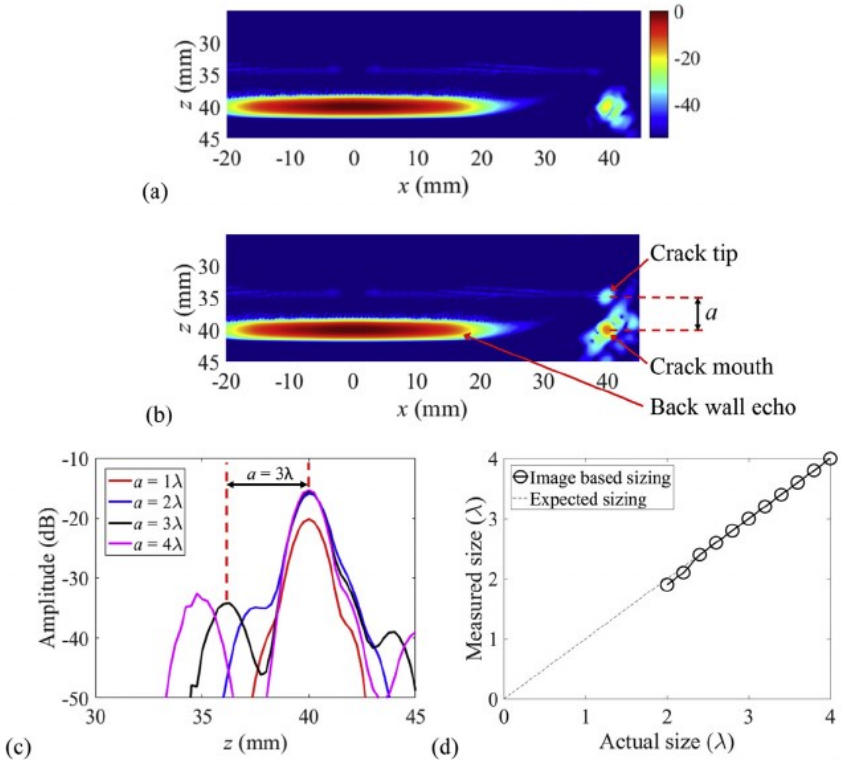

Fig. 2. TFM images from the simulated FMC data for the structure shown in Fig. 1 and a SBC with a size of (a) $a = 0.5\lambda$ and (b) $a = 4\lambda$. (c) Image amplitude distribution along a slice through the crack location for SBCs with various sizes. (d) The measured crack size using the image-based sizing technique against actual size.

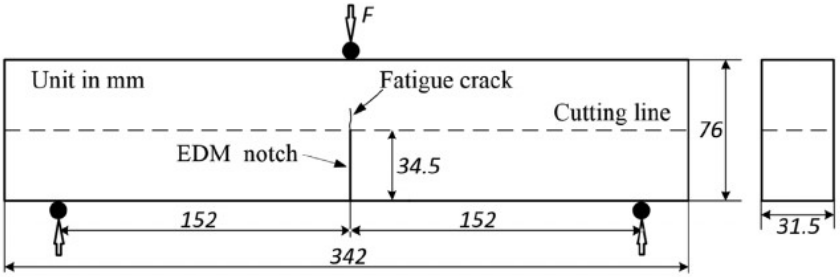

Fig. 4. Geometry of the single-edge notched bend (SENB) specimen for 3-point bending test.

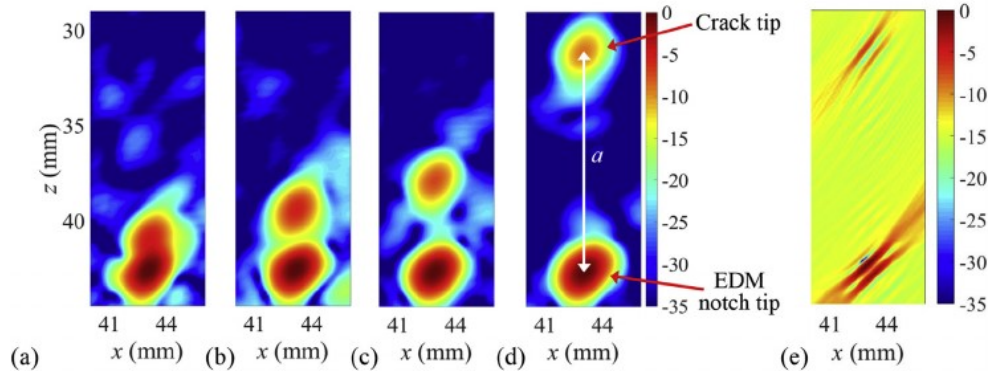

Fig. 5. Fatigue growth monitoring using the 5 MHz ultrasonic array probe at F_{max} = 7.5 kN and a load cycle of (a) 50 k, (b) 85 k, (c) 115 k and (d-e) 195 k. Note that (e) is the TFM image of un-pre-processed data, i.e. without de-noising filter or Hilbert envelope.

measurement and the database is obtained by finding the maximum cross-correlation coefficient and this match is defined as the measured crack size [22]. Here, the database includes cracks with sizes ranging 0.2λ - 3λ with 0.05λ increments. It is noted that this S-matrix method is based on the measured shape of the scattering pattern and hence amplitude calibration is not needed [22].

4. Experimental measurements for real fatigue cracks

4.1. Specimen preparation

In the SBC fabrication process, a single-edge notched bend (SENB) aluminum (2014-T6) specimen of size 342 mm × 76 mm × 31.5 mm, as shown in Fig. 4, is first made following ASTM standard E1820 [34]. An EDM starter notch is cut in the center of the sample to a depth of 34.5 mm using a wire of width 0.1 mm. A fatigue crack is then propagated from the end of the EDM starter notch by subjecting the specimen to 3-point bending test in a fatigue testing machine (Instron 8801). The load is varied from 10% of the maximum load to the maximum load (i.e. load range $0.1F_{max}$ - F_{max}) as a sinusoidal wave with a frequency of 5 Hz. The specimen is finally machined along the dashed line shown in Fig. 4 to remove the EDM notch and leave the fatigue crack. Therefore, the length of the SBC depends on the number of load cycles in the bending test and the remaining thickness of the sample. Using this method, a range of SBCs with different lengths were manufactured and used to examine the performance of the characterisation techniques. It is noted that the maximum load and the load frequency are chosen to simulate possible load conditions in real structures. For example, the load frequency of 5 Hz is equivalent to the load condition on a railway axel when a rail wheel with a diameter 920 mm passes through with a speed of 52 km/h.

4.2. Experimental setup

The three ultrasonic arrays specified in Table 1 (manufactured by Imasonic, Besancon, France) were used in the experiments. An array controller (Micropulse MP5PA, Peak NDT, Ltd., Derby, UK) was used to capture the FMC datasets which were then post-processed on a desktop PC. It is noted that the collected FMC datasets from the 5 MHz and 10 MHz array probes (#1 and #2 ultrasonic array probes specified in Table 1) were used to assess the image-based sizing technique while those from the 2.5 MHz array probe (#3 ultrasonic array probe specified in Table 1) were used for the S-matrix sizing method.

4.3. Fatigue crack growth monitoring using the image-based sizing technique

In the bending fatigue test (F_{max} = 7.5 kN), the crack length was measured every ~20 k cycles using both the ultrasonic image-based and surface optical sizing techniques. It is noted that these measurements were taken in the absence of load and a Gaussian band-pass filter with the same center frequency as the used array probe and 100% fractional bandwidth was used to post-process the FMC array data set before image reconstruction. Ultrasonic images obtained at 5 MHz and 10 MHz are as shown in Figs. 5 and 6 respectively. The higher frequency used in Fig. 6 shows higher image resolution (relative to Fig. 5) from which the crack length can be measured as the distance between the EDM notch tip and the crack tip. It is noted that when the crack is smaller than 2 mm, its size is not resolvable from the images obtained from 5 MHz probe but only those from 10 MHz, as the examples shown in Figs. 5(a) and 6(a). Fig. 7(a) shows an optical view of a typical fatigue crack from which its surface breaking length can be measured and Fig. 7(b) shows how the crack length varies as a function of number of load cycles. Also shown in Fig. 7(b) are the results of 10 MHz image-based sizing (Fig. 6) from which it can be seen that the ultrasonically measured values appear 2–3 mm longer than those measured from the optical image of the surface.

4.4. Fatigue crack profile measurement

In order to better understand influence of the fatigue crack profile on our sizing results, fatigue cracks fabricated using various maximum loads (F_{max}) were completely fractured open under a static load of

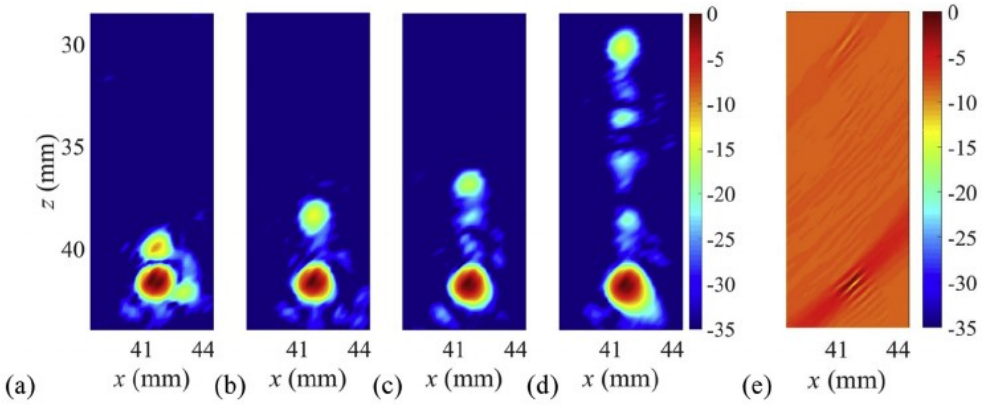

Fig. 6. Fatigue growth monitoring using 10 MHz ultrasonic array probe at F_{max} = 7.5 kN and a load cycle of (a) 50 k, (b) 85 k, (c) 115 k and (d-e) 195 k. Note that (e) is the TFM image of un-pre-processed data, i.e. without de-noising filter or Hilbert envelope.

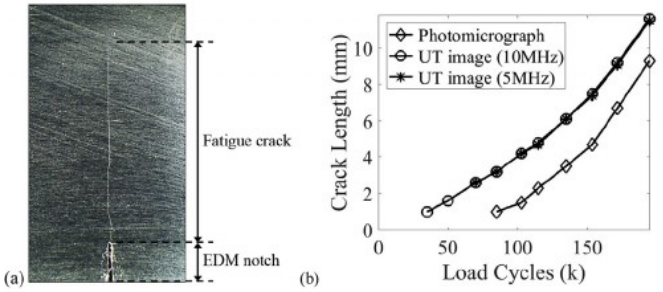

Fig. 7. (a) An optical image of one of the generated fatigue cracks. (b) Comparison of the mesured crack length using the optical image-based and ultrasonic image-based sizing techniques. Note that F_{max} = 7.5 kN in these tests.

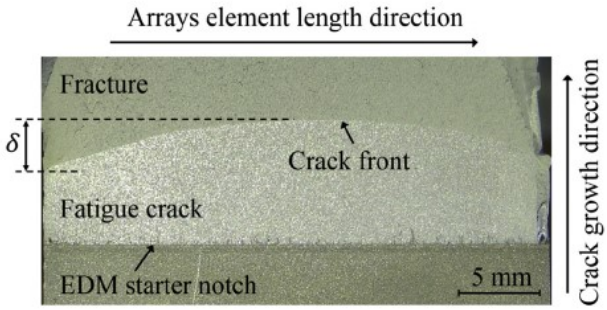

Fig. 8. Optical image of a fatigue crack surface obtained after fracturiug the sample. The sample was fatigued at F_{max} = 7.5 kN for 155 k cycles before being fractured open.

30 kN. Fig. 8 shows an optical image of one such fractured-open sample in which the regions corresponding to the EDM notch, fatigue crack, and fracture can be identified. From Fig. 8 it can be seen that the crack front is curved meaning that there is a length difference, δ, between the crack center and the crack edge. This difference was measured for various samples and was found to vary between 2.5 and 3 mm which explains the previously mentioned difference between the ultrasonic image-based measurement and the optically measured surface crack lengths. The crack surface roughness was also measured at an early crack growth stage (a < 5 mm) using a stylus profilometer (Talysurf, Taylor Hobson, Leicester, UK) and the measured surface roughness was found as, R_a = 10–20 μm.

4.5. Sizing surface breaking cracks

5 specimens with a fatigue crack of length (measured using the ultrasonic image-based technique at 10 MHz) of around 5 mm (generated under different F_{max} and cycles) were machined to remove the EDM notch and only leave the fatigue crack. Further back-wall material was then removed in steps to create cracks from 5 mm to 1.6 mm in length. For example, Fig. 9 shows the crack length measured using the 10 MHz array as the sample was thinned, from which it can be seen that the location of the crack tip remains unchanged but the reflection from the back-wall and crack mouth moves toward the array. Fig. 10(a–c) show the experimentally measured S-matrices obtained using a 2.5 MHz array on the same sample. The corresponding FE-simulated S-matrices from the database that have the highest cross-correlation coefficient are shown in Fig. 10(d–f). In order to explore the measurement errors, the true size was assumed to be that from the 10 MHz images of the large

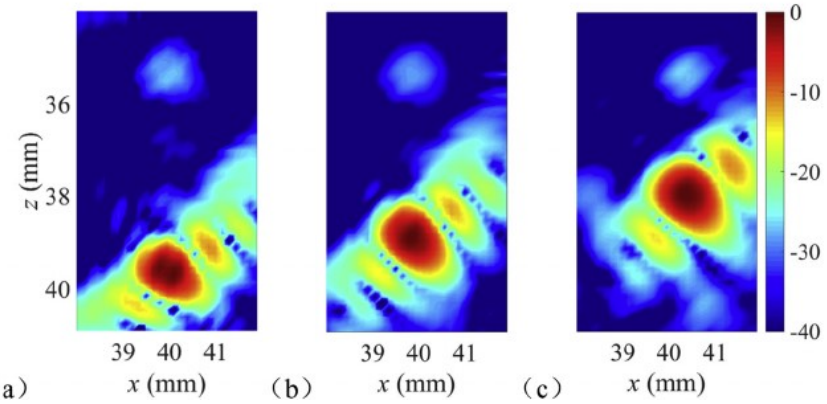

Fig. 9. Experiementally measured 10 MHz ultrasonic images from SBCs with various lengths. The sample was made at F_{max} = 7.5 kN and 100 k load cycles. The measured crack length is; (a) a = 4.6 mm (7.19λ at 10 MHz), (b) a = 3.6 mm (5.63λ at 10 MHz) and (c) a = 2.6 mm (4.06λ at 10 MHz).

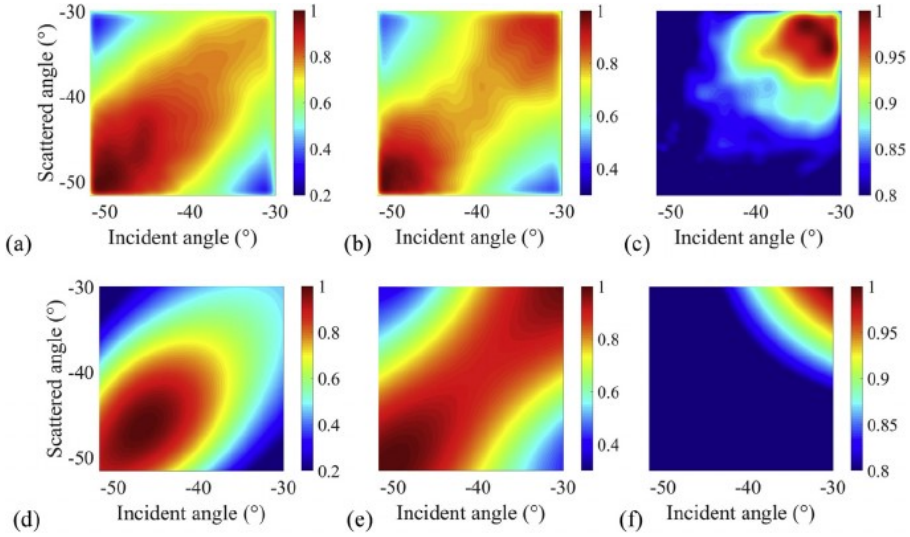

Fig. 10. Comparison of S-matrices obtained from; (a-c) the experimentally measured FMC data set and (d-f) an FE model. Note that in each figure, the amplitude is normalized to its own maximum and shown on a linear scale. The sample was made at F_{max} = 7.5 kN and 100 k load cycles. The measured crack length is; (a,d) a = 4.6 mm (1.80λ at 2.5 MHz), (b,e) a = 3.6 mm (1.41λ at 2.5 MHz) and (c,f) a = 2.6 mm (1.02λ at 2.5 MHz). Note that (a-c) were obtained from the same cracks as used for Fig. 9(a–c).

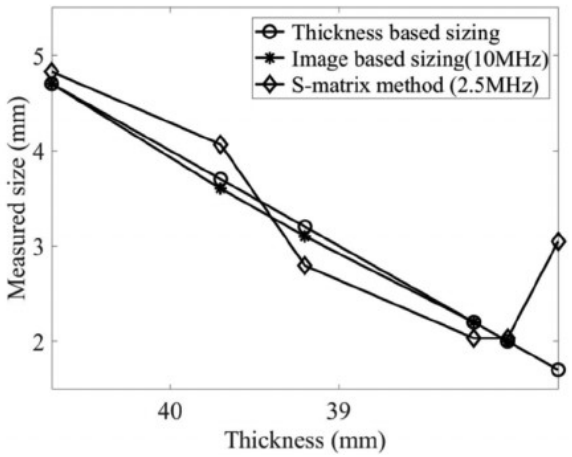

Fig. 11. Experiementally measured crack size from the specimen fabrication under F_{max} = 7.5 kN against the total sample thickness.

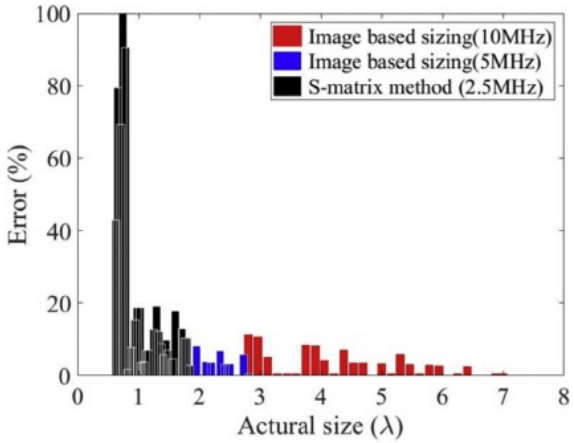

Fig. 12. Experiementally measured sizing errors for real SBCs using both the image-based and the S-matrix sizing techniques.

(5 mm) cracks minus the thickness of the removed material. We note that this assumption leads to some potential erros in the absolute size (as this was extracted from an experimental image) but the erros in measured size change will be small as the material removal is known to high accuracy (i.e. error < 0.1 mm). Fig. 11 compares the ultrasonically measured size against the total sample thickness. The high frequency (10 MHz) image-based sizing result is a straight line of 0.988 gradient (obtained from a least squared fit), strongly suggesting the accurate sizing. The S-matrix method (2.5 MHz) shows only small deviations (< 0.5 mm) from the high frequency image-based results for all cases except for the smallest manufactured crack which is thought to be around 1.9 mm in length (or 0.74λ at 2.5 MHz).

Fig. 12 summarises the image-based and S-matrix-based sizing performance for all the manufactured fatigue samples. Note that the imaging-based sizing technique was also used for the FMC array data sets captured using 5 MHz probe from a few cracks to increase the sizing examination region. As shown in Fig. 12, the image-based sizing technique shows excellent accuracy (sizing errors less than 11%) for SBCs varying in length from 1.95 to 2.81 λ at 5 MHz (i.e. 2.50–3.6 mm) and 2.81–7.34 λ at 10 MHz (i.e. 1.80–4.70 mm) Note that the image-based sizing method cannot be applied to smaller cracks as the crack tip image merges with the crack mouth image at about 2.0λ. However, the S-matrix method shows good accuracy (sizing errors less than 19%) for the smaller cracks, i.e. SBCs varying length from 0.78 to 1.84 λ at 2.5 MHz (i.e. 2.0–4.7 mm). From Fig. 12 it can also be seen that the sizing errors for the very small cracks, i.e. < 0.78λ, becomes very high, and so this represents the lower limit of this sizing technique.

5. Discussion

The effects of surface roughness, crack front profile and crack closure condition on the experimental crack size measurement are now discussed. As mentioned in Section 4.4, the surface roughness of all fabricated fatigue cracks varied from 10 μm to 20 μm which is 0.39%–3.13% respectively of the wavelength of the 2.5 MHz and 10 MHz arrays. The good sizing performance shown in Fig. 12 suggests that this low surface roughness does not significantly affect the crack sizing, except in contributing to the lower limit on the S-matrix technique. This finding is in-line with previous studies on scattering from rough surfaces and sizing of embedded cracks [24–29,35–38]. The crack front profile variation along the array element length direction, as shown in Fig. 8, is thought to explain why the measured length using the ultrasonic image-based sizing technique is around 2.5–3 mm longer than that obtained from the optical images of the specimen surface, i.e. Fig. 7(a). The crack front profile variation could also lead to errors in the S-matrix method as the measurement is from a variable length crack (over the width of the array) and the database assumes a constant crack length (i.e. it is a 2D model). The magnitude of these errors is hard to estimate, however, the relatively good agreement between the experimentally measured and known crack lengths suggest it is a relatively

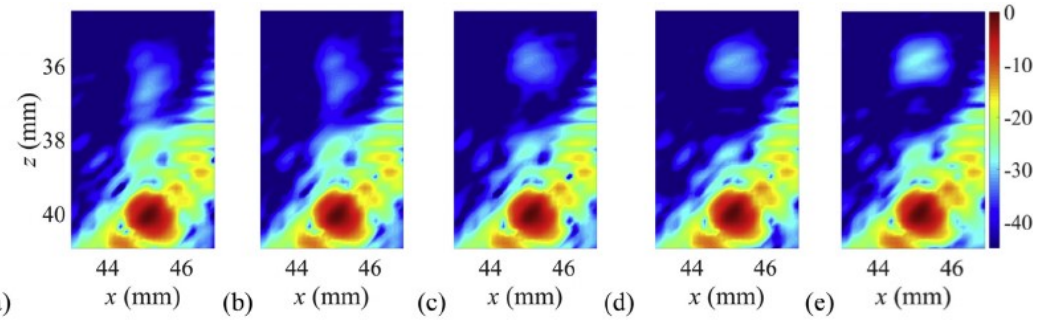

Fig. 13. Experiementally measured ultrasonic images for a SBC under a static crack-opening load of F_s = ; (a-e) 0–4 kN (in 1 kN increments). The sample was made at F_{max} = 7.5 kN and 125 k load cycles.

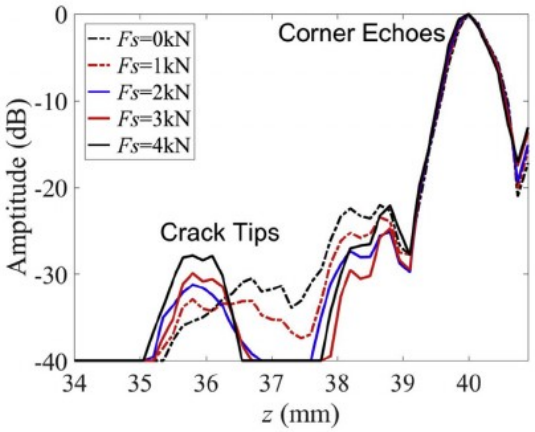

Fig. 14. The image intensity (from Fig. 13) along the thickness direction at x = 45 mm.

small effect for this geometry.

It is known that the fatigue cracks due to bending can be partially closed due to residual stresses after removal of the loading [7]. The effect of this crack closure condition was investigated on a crack with a = 3.4 mm (1.33λ at 2.5 MHz and 5.31λ at 10 MHz) by the application of static loads, F_s = 0–4 kN (varied in 1 kN increments), applied such as to open the crack. In each static load condition, 10 MHz and 2.5 MHz array probes were used to capture the FMC array data sets and sizing was performed using both approaches. Fig. 13 shows images with the 10 MHz array probe and Fig. 14 shows the intensity variation along a vertical line through the crack. From Figs. 13 and 14, it can be seen that the image amplitude at the crack tip increases with crack-opening load. The location of the crack tip image remains unchanged for $F_s < 2$ kN and then moves by around 0.6 mm for $F_s > 2$ kN, suggesting the crack tip is opening. Fig. 15 shows the measured S-matrices for different crack-opening loads, from which it can be seen that the scattering amplitude increases with F_s. It is thought that this is due to the higher static load separating the partial contact along the crack surface, leading to more energy being reflected from solid-air interface. It can also be seen from Fig. 15 that the measured shapes of the S-matrices are relatively unchanged with load which means that the measured crack length (using the database cross-correlation technique) is similarly relatively unchanged as the correlation metric is a measure of shape and is amplitude invariant.

6. Conclusion

The performance of both the ultrasonic image-based sizing technique and the S-matrix database correlation method was demonstrated on real fatigue cracks (length ranging from 0.63λ – 7.34λ). We note that this level of performance is very similar to that previously achieved on EDM notches [18,23]. It was shown that for the SBCs with size greater than 2.0 λ, the image features from the crack tip and mouth could be used to measure the size accurately. For SBCs with size less than 2.0 λ these image features merge together rending image-based

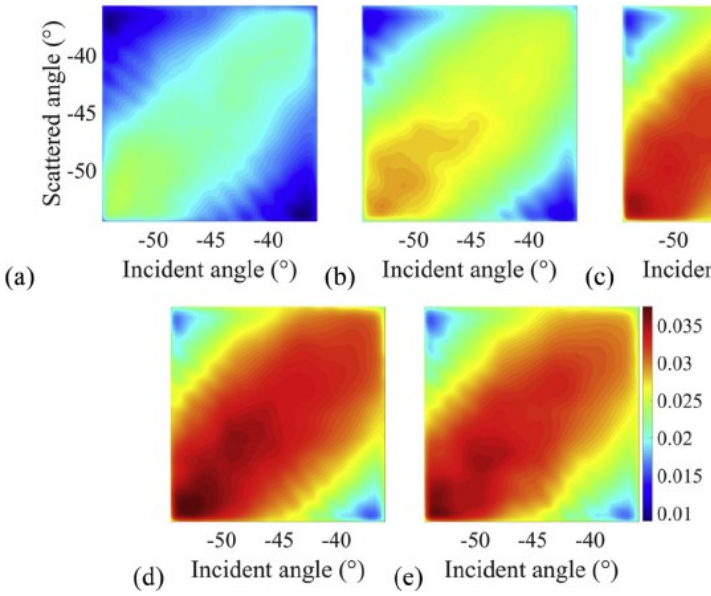

Fig. 15. Experiementally measured S-matrices for the same SBC corresponding to Fig. 13 under a crack-opening static load of F_s = ; (a-e) 0–4 kN (in 1 kN increments). Note that the resultant highest correlation coefficient between the database and (a-e) is; 0.9712, 0.9783, 0.9799, 0.9797 and 0.9786 respectively, suggesting that a good match was found in the database in each case.

sizing inaccurate. However, small cracks of size greater than 0.78λ could still be sized using the experimentally measured S-matrix and cross-correlating this with an S-matrix database which corresponds to smooth SBCs with various sizes, pre-calculated from finite element models.

This good sizing accuracy suggested that the low roughness of the real crack surfaces (i.e. R_a = 0.39–3.13% of the wavelength) had a negligible effect on crack sizing by both techniques. The exception being that the roughness was thought to contribute to the lower limit observed for the S-matrix sizing technique. The reason is that roughness could be expected to lead to small differences with respect to the pre-computed smooth-crack database and these become more significant as the crack gets smaller and the information content of the S-matrix decreases. It is also thought that crack front profile variation can cause measurement errors particularly for the S-matrix method which assumes a 2D model of the crack profile. It was also shown that crack closure caused location errors in the crack tip image and hence affects image-based sizing. The S-matrix method showed measurement robustness in the crack closed condition as it is a measure of the shape of the S-matrix and is amplitude invariant. These findings have the potential to contribute to help the industrial uptake of these emerging array-based crack sizing techniques.

Acknowledgements

This work was supported by the National Science Foundation of China (Grant No. 61501381) and the China Scholarship Council. This work was also supported through the core research programme within the UK Research Center in NDE (RCNDE) funded by EPRSC (Grant No. EP/L022125/1).

Appendix A. Supplementary data

Supplementary data related to this article can be found at http://dx.doi.org/10.1016/j.ndteint.2018.06.005.

References

[1] Collins JA. Failure of materials in mechanical design: analysis, prediction, prevention. New York: John Wiley & Sons Inc; 1993.
[2] Sieradzki K, Newman RC. Stress-corrosion cracking. J Phys Chem Solid 1987;48:1101–13.
[3] Woodtli J, Kieselbach R. Damage due to hydrogen embrittlement and stress corrosion cracking. Eng Fail Anal 2000;7:427–50.
[4] Cherfaoui M. Innovative techniques in non-destructive testing and industrial applications on pressure equipment. Procedia Eng 2012;46:266–78.
[5] Klinger C, Bettge D. Axle fracture of an ICE3 high speed train. Eng Fail Anal 2013;35A:66–81.
[6] William CD. Materials science and engineering—an introduction. New York: John Wiley & Sons Inc; 1997.
[7] Schijve J. Fatigue of structures and materials. Dordrecht: Springer; 2009.
[8] Almonda DP, Li T, Rees DAS, Weekes B, Wilson J, Tian GY. Thermographic techniques for the detection of cracks in metallic components. Insight 2011;53:614–20.
[9] Quaegebeur N, Bouslama N, Bilodeau M, Guitel R, Masson P, Maslouhi A, Micheau P. Guided wave scattering by geometrical change or damage: application to characterization of fatigue crack and machined notch. Ultrasonics 2017;73:187–95.
[10] Yang J, He J, Guan X, Wang D, Chen H, Zhang W, Liu Y. A probabilistic crack size quantification method using in-situ Lamb wave test and Bayesian updating. Mech Syst Signal Process 2016;78:118–33.
[11] Wang D, He J, Guan X, Yang J, Zhang W. A model assessment method for predicting structural fatigue life using Lamb waves. Ultrasonics 2018;84:319–28.
[12] He J, Guan X, Peng T, Liu Y, Saxena A, Celaya J, Goebel K. A multi-feature integration method for fatigue crack detection and crack length estimation in riveted lap joints using Lamb waves. Smart Mater Struct 2013;22:105007.
[13] Satyarnarayan L, Pukazhendhi DM, Balasubramaniam K, Krishnamurthy CV, Ramachandramuthy DS. Phased array ultrasonic measurement of fatigue crack growth profiles in stainless steel pipes. J. Pres. Ves Tech-Trans ASME 2007;129:737–43.
[14] Prager J, Kitze J, Acheroy C, Brackrock D, Brekow G, Kreutzbruck M. SAFT and TOFD—a comparative study of two defect sizing techniques on a reactor pressure vessel mock-up. J Nondestr Eval 2013;32:1–13.
[15] Holmes C, Drinkwater BW, Wilcox PD. Post-processing of the full matrix of ultrasonic transmit-receive array data for non-destructive evaluation. NDT E Int 2005;38:701–11.
[16] Zhang J, Drinkwater BW, Wilcox PD, Hunter A. Defect detection using ultrasonic arrays: the multi-mode total focusing method. NDT E Int 2010;43:123–33.
[17] Bannouf S, Robert S, Casula O, Prada C. Data set reduction for ultrasonic TFM imaging using the effective aperture approach and virtual sources. J Phys Conf 2013;457(012007).
[18] Felice MV, Velichko A, Wilcox PD. Accurate depth measurement of small surface-breaking cracks using an ultrasonic array post-processing technique. NDT E Int 2014;68:105–12.
[19] Zhang J, Yu P, Gang T. Measurement of the ultrasonic scattering matrices of near-surface defects using ultrasonic arrays. Nondestr Test Eval 2016;31:303–18.
[20] Tant K, Mulholland A, Gachagan A. A model-based approach to crack sizing with ultrasonic arrays. IEEE Trans Ultrason Ferroelectrics Freq Contr 2015;62:915–26.
[21] Shakibi B, Honarvar F, Moles MDC, Caldwell J, Sinclair AN. Resolution enhancement of ultrasonic defect signals for crack sizing. NDT E Int 2012;52:37–50.
[22] Zhang J, Drinkwater B, Wilcox P. Defect characterization using an ultrasonic array to measure the scattering coefficient matrix. IEEE Trans Ultrason Ferroelectrics Freq Contr 2008;55:2254–65.
[23] Zhang J, Drinkwater B, Wilcox P. The use of ultrasonic arrays to characterize crack-like defects. J Nondestr Eval 2010;29:222–32.
[24] Zhang J, Drinkwater B, Wilcox P. Effect of roughness on imaging and sizing rough crack-like defect using ultrasonic arrays. IEEE Trans Ultrason Ferroelectrics Freq Contr 2012;59:939–48.
[25] Sinclair AN, Fortin J, Shakibi B, Honarvar F, Jastrzebski M, Moles MDC. Enhancement of ultrasonic images for sizing of defects by time-of-flight diffraction. NDT E Int 2010;43:258–64.
[26] Camachoa J, Atehortuab D, Cruzaa JF, Brizuelac J, Ealob J. Ultrasonic crack evaluation by phase coherence processing and TFM and its application to online monitoring in fatigue tests. NDT E Int 2018;43:258–64.
[27] Chassignole B, El Guerjouma R, Ploix M-A, Fouquet T. Ultrasonic and structural characterization of anisotropic austenitic stainless steel welds: towards a higher reliability in ultrasonic non-destructive testing. NDT E Int 2010;43:273–82.
[28] Newhouse VL, Bilgutay NM, Saniie J, Furgason ES. Flaw-to-grain echo enhancement by split-spectrum processing. Ultrasonics 1982;20. 59–58.
[29] Saniie J, Oruklu E, Yoon S. System-on-Chip design for ultrasonic target detection using split-spectrum processing and neural networks. IEEE Trans Ultrason Ferroelectrics Freq Contr 2012;59:1354–68.
[30] Schmerr LW. Fundamentals of ultrasonic nondestructive evaluation - a modeling approach. New York: Prenum press; 1998.
[31] Velichko A, Wilcox PD. Thompson DO, Chimenti DE, editors. Efficient finite element modelling of elastodynamic scattering from near surface and surface breaking defects," in Review of Progress in QNDE, 30, vols. 59–66. Melville, NY: American Institute of Physics; 2010.
[32] Miller FG, Pursey H. The field and radiation impedance of mechanical radiators on the free surface of a semi-infinite isotropic solid. Proc Roy Soc Lond 1954;34:521–41.
[33] Krautkramer J, Krautkramer H. Ultrasoinc testing of materials. New York: Springer Verlag; 2003.
[34] ASTME1820. Standard test method for measurement of fracture toughness. American Society for Testing and Materials; 2011.
[35] Ogilvy JA. Model for the ultrasonic inspection of rough defects. Ultrasonics 1989;27:69–79.
[36] Ogilvy JA. Elastic model for simulating ultrasonic inspection of smooth and rough defects. Ultrasonics 1991;29:490–6.
[37] Shi F, Lowe MJS, Xi X, Craster RV. Diffuse scattered field of elastic waves from randomly rough surfaces using an analytical Kirchhoff theory. J Mech Phys Solid 2016;92:260–77.
[38] Pettit JR, Walker AE, Lowe MJS. Improved detection of rough defects for ultrasonic nondestructive evaluation inspections based on finite element modelling of elastic wave scattering. IEEE Trans Ultrason Ferroelectrics Freq Contr 2015;62:1797–808.